frontiers in Materials

ORIGINAL RESEARCH
published: 14 August 2020
doi: 10.3389/fmats.2020.00287

The BCC-FCC Phase Transformation Pathways and Crystal Orientation Relationships in Dual Phase Materials From Al-(Co)-Cr-Fe-Ni Alloys

Ulrike Hecht[1], Sergej Gein[1], Oleg Stryzhyboroda[1], Eyal Eshed[2] and Shmuel Osovski[2]*

[1] Access e.V., Aachen, Germany, [2] Technion-Israel Institute of Technology, Faculty of Mechanical Engineering, Haifa, Israel

The alloy system Al-(Co)-Cr-Fe-Ni contains compositional ranges where a solid state BCC-FCC phase transformation leads to dual-phase materials composed of face-centered cubic (FCC) and body-centered cubic (BCC) phases with nearly equal volume fraction. The microstructure arising from this transformation at slow cooling rates is the classical Widmanstätten structure, with FCC-laths and colonies growing from grain boundaries into the parent BCC-B2 grain. Very distinct microstructures are obtained, when Widmanstätten growth is kinetically suppressed e.g., during continuous cooling with high cooling rates. These novel microstructures are associated with the spinodal decomposition of the parent BCC-B2 such that FCC growth occurs during the spinodal decomposition or upon annealing from a metastable, fully spinodal state. We review the microstructures at case as function of the imposed cooling regimes for the Co-free medium entropy alloy $AlCrFe_2Ni_2$. One of them, termed ultrafine vermicular microstructure, involves a characteristic and novel crystal orientation relationship (OR) between FCC and BCC. We identify the common planes and directions of this OR using electron backscatter diffraction maps to be $\{111\}^{FCC} \parallel \{12\bar{1}\}^{BCC}$ and $\langle\bar{1}01\rangle^{FCC} \parallel \langle\bar{1}0\bar{1}\rangle^{BCC}$, respectively. Embedded is a second OR with $\{1\bar{3}\bar{1}\}^{FCC} \parallel \{\bar{1}03\}^{BCC}$ and $\langle101\rangle^{FCC} \parallel \langle010\rangle^{BCC}$. We further show that the vermicular FCC phase contains a high amount of lattice strain and sub-grain boundaries with disorientation angles in the range from 2 to 12°, as a result of the solid-state phase transformation.

Keywords: high entropy alloy, medium entropy alloys, phase transformation pathways, crystal orientation relationships, dual phase materials

OPEN ACCESS

Edited by:
Liqiang Wang,
Shanghai Jiao Tong University, China

Reviewed by:
Liang Zhang,
Chongqing University, China
Xinwang Liu,
Huazhong University of Science & Technology, China

****Correspondence:***
Ulrike Hecht
u.hecht@access-technology.de

Specialty section:
This article was submitted to Structural Materials, a section of the journal Frontiers in Materials

Received: *31 May 2020*
Accepted: *29 July 2020*
Published: *14 August 2020*

Citation:
Hecht U, Gein S, Stryzhyboroda O, Eshed E and Osovski S (2020) The BCC-FCC Phase Transformation Pathways and Crystal Orientation Relationships in Dual Phase Materials From Al-(Co)-Cr-Fe-Ni Alloys. Front. Mater. 7:287. doi: 10.3389/fmats.2020.00287

INTRODUCTION

High entropy and medium entropy alloys attracted wide interest, driven by the quest for multicomponent, yet single phase materials with face-centred-cubic (FCC), body-centred-cubic (BCC) and hexagonal-close-packed (HCP) structures while eliminating secondary (and tertiary) phases (Steurer, 2020). More recently, research on dual-phase (or multi-phase) materials gained momentum, because their heterophase nature allows tailoring mechanical properties and achieving well-balanced property profiles (Bönisch et al., 2018). The quinary alloy system of major interest is

Al-Co-Cr-Fe-Ni offering a composition range for dual-phase alloy design around $Al_xCoCrFeNi$ with $0.5 < x < 0.9$ (Kao et al., 2009; Wang et al., 2014, Gangireddy et al., 2019). The dual-phase alloys provide considerable strength while retaining about ∼20% tensile ductility (Gangireddy et al., 2019) and also show promising corrosion resistance, comparable to stainless steels (Shi et al., 2017). Since alloy design strategies attach increasing importance to cost reduction and resource-conserving aspects, the quaternary alloy system Al-Cr-Fe-Ni proved equally prolific around compositions $AlCrFe_2Ni_2$ (Dong et al., 2016 and Li et al., 2020) thus avoiding expensive and resource-critical elements like Cobalt (Tkaczyk et al., 2018).

Alloys like $Al_{0.7}CoCrFeNi$, $Al_{0.8}CoCrFeNi$ and certainly many other alloys with reduced or fully eliminated Co content like $AlCrFe_2Ni_2$, are dual-phase materials composed of FCC and BCC phases with nearly equal volume fraction, typically with a Widmanstätten lath morphology of the FCC phase (De Jeer et al., 2017; Abuzaid and Sehitoglu, 2018). This microstructure type, known as "duplex microstructure", is similar though not identical to the one well known from duplex steels (Ohmori et al., 1995; Knyazeva and Pohl, 2013). The major difference relates to the nature of the parent BCC phase, being a disordered d-ferrite (BCC-A2) in the case of duplex steels but an ordered BCC-B2 phase in the case of Al-(Co)-Cr-Ni alloys. The most remarkable and eminently important difference arises from the limited stability of this BCC-B2 phase, which is prone to spinodal decomposition into a Fe, Cr- rich BCC-A2 phase and a Ni, Al-rich BCC-B2 phase. The domain ordering of the BCC-B2 in the spinodally decomposed state was investigated in detail by Linden et al. (2017), while also accounting for microsegregation inherited from solidification.

The spinodal decomposition of the BCC-B2 phase and more specifically its interaction with the BCC-FCC phase transformation is one of the most fascinating aspects in the alloy system Al-(Co)-Cr-Fe-Ni, leading to novel phase transformation pathways and unique microstructures. The purpose of this paper is to accurately describe the distinct transformation pathways for distinct cooling regimes, while referring to the most recent thermodynamic data. Emphasis is placed on the crystal orientation relationships (ORs) established between the BCC and FCC phases. We will introduce a new crystal OR, which pertains to a novel and unique microstructure termed "ultrafine vermicular microstructure" (UVM). Vermicular structures have first been reported in Dong et al. (2016) for an as cast $AlCrFe_2Ni_2$ alloy, but are likewise forming in $Al_{0.7}CoCrFeNi$, $Al_{0.8}CoCrFeNi$ at sufficiently high cooling rates, e.g., during permanent mold casting. Dong et al. (2016) described this microstructure as "noodle-like", but gave no explanation about its origin, while alluding to a "eutectic" design principle. The microstructure captured our attention because it compares to no other structure that we saw in many years of research on different metallic and intermetallic materials. We thus engaged into an ample experimental investigation, also including further alloy design, heat treatments and mechanical property characterization, as presented by S. Gein et al. in this Frontier's edition.

This paper focuses on microstructure characterization only, being structured as follows: the experimental methods used for sample preparation and microstructure characterization are briefly described in section 2; an overview on the distinct dual-phase microstructures and the associated phase transformation pathways are described in section 3. The newly identified crystal orientation relationship pertaining to ultrafine vermicular microstructures is presented with due details in section 3. Finally, a short summary and main conclusion are given in section 4.

EXPERIMENTAL METHODS OF SAMPLE PREPARATION AND CHARACTERIZATION

Samples presented in section 3 and 4 were prepared by arc melting under Argon gas (Ar6.0) in an Edmund Bühler device type AM500 using elemental mixtures of the desired alloy composition close to $AlCrFe_2Ni_2$. The melted and solidified buttons of 50 and 300 g each were flipped and repeatedly molten for at least 3 times, to insure chemical homogeneity. The elements used for alloy preparation had a purity of at least 99.98 wt-%. For completeness of the overview on the distinct dual-phase microstructures we also present a sample which was produced by additive manufacturing using powder bed fusion (L-PBF) in order to reach high cooling rates i.e., $>10^3$ K/min. The L-PBF sample was provided by Oerlikon AM GmbH in the as-build condition and was further annealed under Argon (Ar4.8) in a horizontal tube furnace at 950°C for a duration of 6 h followed by water quenching.

Sample characterization encompassed microstructure analysis in a scanning electron microscope SEM type Zeiss Gemini 1550 equipped with energy dispersive X-ray analysis (EDS) and electron backscatter diffraction (EBSD) detectors. The EDS-spectra and EBSD-patterns were acquired and analyzed using the Oxford-INCA software. Samples for microstructure characterization in SEM were cut from the arc melted buttons, embedded in conductive resin, grinded and polished. After standard polishing steps a final step of vibratory polishing (Buehler VibroMet 2) was applied, which allows acquiring good Kikuchi patterns during EBSD mapping.

Selected samples were investigated by conventional transmission electron microscopy (TEM) and scanning transmission electron microscopy (STEM) including energy dispersive X-ray analysis. TEM images and selected area electron diffractions (SAED) were obtained using a FEI Tecnai G2 T20 200 KeV TEM with a LaB6 electron source. A Titan Themis G^2 60–300 (FEI/Thermo Fisher) was used for high resolution STEM Imaging and EDS maps. **Samples for** microstructure characterization in TEM and STEM were prepared by focused ion beam cutting (FIB) of thin lamellae using a dual-beam FEI Helios NanoLab G3 scanning microscope.

DUAL-PHASE MICROSTRUCTURES IN AL-(CO)-CR-FE-NI ALLOYS

Three very distinct dual-phase microstructures evolve upon cooling certain Al-(Co)-Cr-Fe-Ni alloys, whenever the alloy

composition is such that two solid-state transformations are involved along the transformation pathway, the allotropic transformation BCC-B2 → FCC-A1 and the spinodal decomposition BCC-B2 → BCC-A2# + BCC-B2#. In the following, we describe the formation of these microstructures and highlight their characteristic morphological features based on the alloy composition $AlCrFe_2Ni_2$. For sake of clarity, the hash symbol is used to denote the product phases of the spinodal decomposition and the Strukturbericht designations A1, A2 and B2 are used in addition to the crystal structure type, as to distinguish ordered (B2) from disordered (A2) BCC phases. The presented information is essentially drawing on results from many experiments with distinct cooling rates, e.g., casting into ceramic and permanent molds, arc melting of buttons with different size (weight) and suction casting, additive manufacturing etc., which are not presented in detail. The typical cooling rates reported in literature range from ∼20 K/min (sand and ceramic mold casting), ∼200 K/min (permanent mold casting), ∼2000 K/min (suction casting) and above $\sim 10^4$ K/min for laser based additive manufacturing.

As will be seen, the term "dual-phase" used to describe FCC-BCC microstructures is not strictly correct, because the BCC phase decomposes spinodally into two BCC-phases with distinct composition sets. However, the vast majority of literature, i.e., De Jeer et al., 2017; Abuzaid and Sehitoglu, 2018, Gangireddy et al., 2019, uses this term, since it is simple and captures the quintessence.

Dual-Phase Microstructures and Associated Phase Transformation Pathways

An overview of characteristic dual-phase microstructures is displayed in **Figure 1** for the Co-free alloy $AlCrFe_2Ni_2$, along with schematic icons of the microstructure and a sketch of the related phase transformation pathways. Other alloys with similar transformation pathways will develop similar microstructure features and indeed we observed them in alloy $Al_xCoCrFeNi$ alloys with $0.7 < x < 0.8$ without showing them in detail. Three distinct dual-phase structure types can be distinguished, being labeled CWM, UVM, and UMM, respectively. They all form from the BCC-B2 parent phase as described below:

(1) The conventional Widmanstätten microstructure (CWM) is formed at low cooling rates, typically less than ∼50 K/min, by diffusion controlled growth of FCC-A1 plates into the parent BCC-B2 grains. The FCC-A1 plates originate from FCC-A1 films at grain boundaries of BCC-B2 and grow into the volume of the grains with a plate-like morphology forming colonies of parallel plates. For other nucleation scenarios a pattern of intersecting plates may develop. Growth requires a small undercooling below the BCC-B2 → FCC-A1 transformation temperature. FCC-A1 growth thus occurs before the spinodal decomposition of the BCC-B2 parent grains. The remaining BCC-B2 phase, located in between the FCC laths will later decompose spinodally into BCC-B2#2 and BCC-A2#. The sequence of phase transformations along the CWM transformation pathway reads:

Pathway (1): BCC-B2 → FCC-A1 + BCC-B2 → FCC-A1 + BCC-B2# + BCC-A2#

The group from the University of Groningen (Rao et al., 2016; De Jeer et al., 2017) investigated the crystallographic orientation relationship between FCC-A1 and BCC (BCC-B2# + BCC-A2#) in a sample from alloy $Al_{0.7}CoCrFeNi$ with Widmannstätten microstructure. The authors report a continuum from the Pitsch OR to the Kurdjumov-Sachs OR. Our own measurements in CWM-samples form alloys $AlCrFe_2Ni_2$, $Al_{0.7}CoCrFeNi$ and $Al_{0.8}CoCrFeNi$ show the Nishiyama-Wassermann OR (Nishiyama, 1934; Wassermann, 1935) extending to the Kurdjumov-Sachs OR (Kurdjumow and Sachs, 1930). This is quite similar to Bunge et al. (2003) who reported a similar spread of ORs in an iron meteorite with Widmanstätten structure formed during the FCC → BCC phase transformation.

(2) The ultrafine vermicular microstructure (UVM) was reported as a "noodle-like" structure by Dong et al. (2016), but its formation and morphological peculiarities have not been described, leaving room to speculations about its origins. Some authors alluded to possible eutectic or eutectoid reactions, simply because the structure is ultrafine and vaguely lamellar in appearance. Our own research shows that this microstructure forms at moderate to high cooling rates, typically ranging from ∼100 K/min to ∼1000 K/min such that Widmanstätten growth is kinetically suppressed. Under these conditions, the undercooling below the BCC-B2 → FCC-A1 transformation temperature increases to some 10 to 100 K eventually going below the binodal line of the phase diagram. The spinodal decomposition of the BCC-B2 phase then triggers the growth of FCC-A1, in what we call a "*duplex spinodal reaction*". The associated transformation pathway reads:

Pathway (2): BCC-B2 → FCC-A1 + BCC-B2# + BCC-A2#

It is currently unclear whether the transformation is fully or at least partly diffusion controlled, given the small length scales involved and the elevated transformation temperature around ∼1000°C. It is, however, possible that the structural transformation to FCC-A1 precedes the chemical part of the transformation. More research is required to clarify this aspect. The most remarkable feature is, however, the ultrafine size of the vermicular FCC-A1 phase, typically with a thickness of about 200 to 500 nm, which is slightly above the wavelength of the spinodal decomposition. We thus propose that the formation of the ultrafine vermicular structure requires large undercooling below the BCC-B2 → FCC-A1 transformation temperature and some limited undercooling below the binodal line and into the three phase field "FCC-A1 + BCC-B2# + BCC-A2#". The ultrafine vermicular microstructure displays special and characteristic morphological features, including a

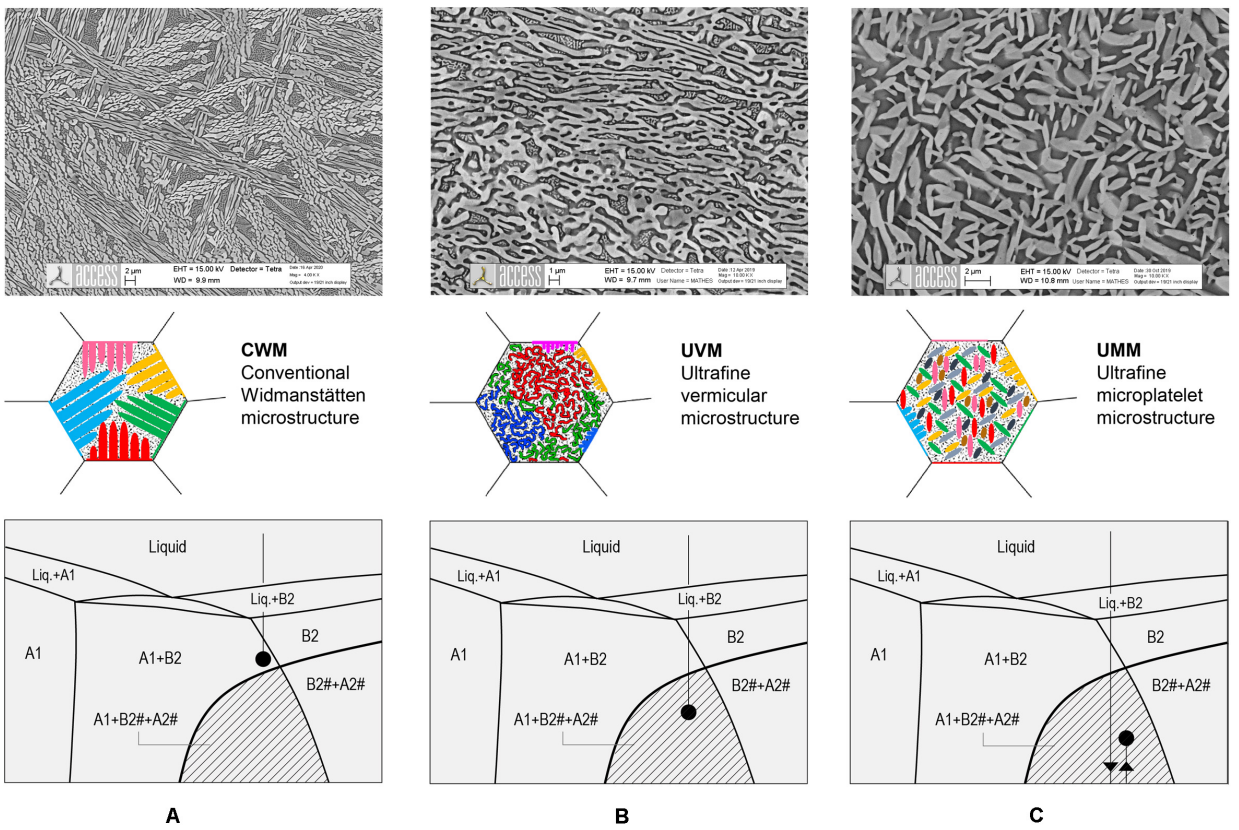

FIGURE 1 | Overview of dual phase microstructures forming in Al-(Co)-Cr-Fe-Ni alloys from the parent BCC-B2 phase under different cooling regimes. The cooling rate increases from left to right. According to the morphology of the FCC phase we distinguish **(A)** classical Widmanstätten laths and colonies, **(B)** ultrafine vermicular network and **(C)** ultrafine micro-platelets. The colors in the icons represent different crystal orientations of the FCC phase inside one parent BCC-B2 grain. The corresponding transformation pathways are schematically depicted on simplified phase diagram sections. The micrographs in the top row are taken from $AlCrFe_2Ni_2$ samples produced by arc melting of 300 g buttons **(A)**, 50 g buttons **(B)** and laser powder bed fusion, L-PBF, with a post-build heat treatment at 950°C/6 h **(C)**.

pronounced contiguity of the FCC-A1 phase, which appears fully interwoven with the spinodally decomposed BCC phase at nearly equal phase fractions. Furthermore, it is associated with a novel crystallographic orientation relationship. Sections 3.1 and section 4 contain more details about this special dual-phase microstructure.

(3) The formation of the ultrafine micro-platelet microstructure (UMM) requires highest cooling rates, e.g., above 1000 K/min and forms only during annealing heat treatments after cooling. Cooling itself must be so fast, that formation of FCC-A1 is fully suppressed, leaving behind a metastable and spinodally decomposed BCC microstructure (BCC-A2# + BCC-B2#). Precipitation of FCC-A1 occurs by isothermal annealing at a temperature in the three-phase field "FCC-A1 + BCC-B2# + BCC-A2#". Our observations show that the metastable spinodal structure offers a high density of nucleation sites for the FCC-A1 phase, such that micro-platelets with distinct crystal orientations form in high number. In fact all 12 variants of the crystallographic OR (Nishiyama-Wassermann) are present. The phase transformation pathway is as follows:

Pathway (3): BCC-B2 → BCC-B2# + BCC-A2# → FCC-A1 + BCC-B2# + BCC-A2# (annealing)

This topical Frontier's edition contains more details about this structure obtained along additive manufacturing routes with post-build annealing, as described by D. Vogiatzief et al. and V. Rocio Molina Ramirez et al. We point out, that nucleation triggered by the compositional modulations of a spinodal decomposition occurs in Fe-Mn alloys, being confined to crystalline defects (Da Silva et al., 2018). Furthermore, Loh et al., 2017 reported spinodal decomposition as the first step in a multistep nucleation of gold and silver nanocrystals in aqueous solutions.

We would like to remark that in a sample or cast part the conventional Widmanstätten structure may coexist with the ultrafine vermicular structure for moderate cooling rates. These mixed structures form successively during continuous cooling with the 1st generation of Widmanstätten plates being well developed along pathway (1), while the remaining BCC-B2 transforms to the ultrafine vermicular microstructure following pathway (2). We summarize this section with pointing out that

the ultrafine vermicular microstructures as well as the micro-platelet microstructures are unique and have not been reported for other alloy systems. Their formation requires the spinodal decomposition of BCC-B2 to trigger the nucleation and growth of FCC-A1. From a thermodynamic point of view their formation requires that a three-phase field "FCC-A1 + BCC-B2# + BCC-A2#" exists in the phase diagram in the region corresponding to the alloy composition. The subject is new, calling for modeling and simulation at all scales.

Ultrafine Vermicular Microstructure in $AlCrFe_2Ni_2$

The nearly fully UVM is obtained in small arc melted buttons (50 g) of alloy $AlCrFe_2Ni_2$, as displayed in **Figure 2**. **Table 1** lists the integral alloy composition measured by EDS. The SEM image in **Figure 2A** reveals three grains with one of the grain boundaries showing a narrow region of Widmanstätten laths protruding from the boundary into one grain. The bright phase with vermicular morphology is FCC-A1, while the dark phase is spinodally decomposed BCC-B2. The inserted micrograph taken at higher magnification shows that the width of the FCC phase in the vermicular network is about the size of the spinodal wavelength. The TEM images in **Figure 2B** show a close-up view of the microstructure constituents: the bright FCC-A1 phase is as small as ∼250 nm in width and contains sub-grains as well as a high density of dislocations; the dark "matrix" phase is spinodally decomposed into an Al-,Ni- rich BCC-B2# (labeled ①) and Cr-, Fe- rich BCC-A2# particles (labeled ②). The diffraction patterns of the two BCC phases are equally displayed for a < 100 > zone axis. A subtle difference in the intensity of the {100} planes, relative to the {110} planes, was observed when comparing the diffractions of the BCC-B2# and BCC-A2# phases. **Table 2** lists the measured phase compositions and lattice parameters for the three phases. The structural features are similar to the ones reported in Dong et al. (2016).

TABLE 1 | Chemical composition of the alloy $AlCrFe_2Ni_2$ measured by EDS in an SEM.

Element	Al	Cr	Fe	Ni
Nominal (at %)	16.67	16.67	33.34	33.34
Mean, Std. dev. (at %)	16.6 ± 0.3	17.4 ± 0.2	33.1 ± 0.3	32.9 ± 0.2
Mean, Std. dev. (wt %)	8.7 ± 0.1	17.7 ± 0.1	36.0 ± 0.3	37.7 ± 0.3

TABLE 2 | Chemical composition and lattice parameters of the phases in an as-cast $AlCrFe_2Ni_2$ sample with ultrafine vermicular microstructure, measured by high resolution EDS in STEM.

Phase	Phase composition, at % (TEM, HR-EDS)				Lattice parameter, a, Å
	Al	Cr	Fe	Ni	
FCC-A1	8.3	19.7	43.5	28.5	a = 3.554
BCC-B2	34.3	3.1	15.1	47.5	a = 2.889
BCC-A2	6.1	32.2	48.5	13.3	not analyzed

CRYSTAL ORIENTATION RELATIONSHIP PERTAINING TO ULTRAFINE VERMICULAR MICROSTRUCTURES

EBSD mapping was used extensively in order to identify the crystal orientation relationship (OR) between the vermicular

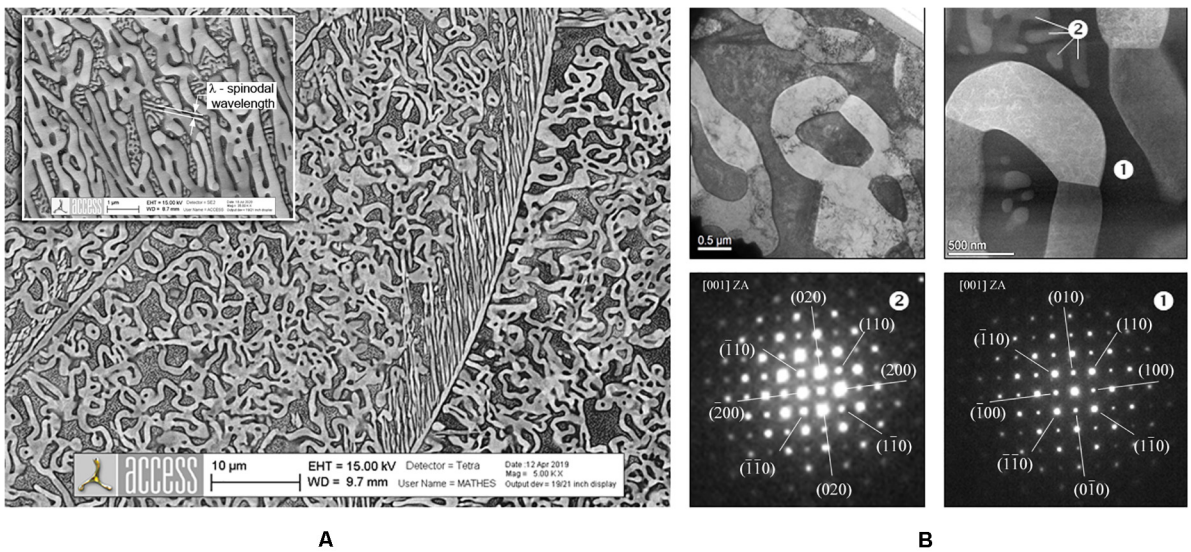

FIGURE 2 | SEM **(A)** and BFTEM as well as STEM **(B)** micrographs of an as-cast $AlCrFe_2Ni_2$ sample featuring the ultrafine vermicular microstructure of FCC-A1 in a spinodally decomposed BCC matrix. The product phases of the spinodal decomposition are labeled ① (BCC-B2#) and ② (BCC-A2). Diffraction patterns taken along a [001] zone axis show subtle difference in the intensity of the {100} planes, relative to the {110} planes, when comparing BCC-B2# and BCC-A2# phases. Note the high dislocation density in the FCC-A1 phase as well as sub-grain boundaries.

FCC and the parent BCC phase, which in turn is spinodally decomposed into a mixture of BCC#1 = BCC-B2 and BCC#2 = BCC-A2 phases. The product phases of the spinodal reaction have different composition and lattice parameter, but identical crystal orientation, and hence no distinction between is made between them. The phases used for mapping were Iron (BCC, space group no. 229) and Nickel (FCC, space group no. 225).

We illustrate the EBSD mapping and results of the analysis based on a mapping region with an area S_a = 1384.384 μm^2 (**Figure 3**) scanned with a resolution of 1 pixel = 0.007 μm^2. The mapping region contains two distinct grains with vermicular microstructure, separated by a grain boundary. A thin FCC film decorates the grain boundary between the neighboring grains. A narrow region of FCC Widmanstätten laths with the crystal orientation of grain 2 grow from the boundary into the opposite BCC grain, i.e., grain 1. For convenience, the crystal mimic of the involved phases is equally depicted. It is noted here, and will be outlined later in more detail, that the FCC phase displays considerable lattice strain and a high density of low angle grain boundaries (LAGBs) with disorientation angles ranging from 2 to 12 degree. Accordingly, the FCC crystal orientation in each grain is rather broadly scattered around a specific average orientation and the FCC pole figures show wider poles compared to the BCC phase, as seen in **Figures 4**, **5**. The two figures display selected pole figures for grain 1 and grain 2, respectively, which illustrate the crystal orientation relationship between vermicular FCC and the parent BCC. It turns out that this is a novel crystallographic OR, which is not only distinct from the ORs observed in samples with classical Widmanstätten (CWM) or ultrafine micro-platelet (UMM) structure, but also different from all other ORs reported for the BCC/FCC systems. In fact, before identifying the new OR we first performed a careful verification of the known ORs, which have been reviewed and tabulated e.g., in (Verbeken et al., 2009).

The new OR described below was found in many samples from different alloys including not only $AlCrFe_2Ni_2$ but also $Al_{0.8}CoCrFeNi$ and $AlCrFe_2Ni_2$ with Mo additions. It is characteristic for dual-phase medium and high entropy alloys with ultrafine vermicular microstructure; we found no exception from it.

Figure 4A shows the relevant pole figures for grain 1 and highlights the poles which correspond to the common planes and directions of the OR. Common planes and directions are indexed and marked in green color with full and dotted circles, respectively. In grain 1 the two crystals imbricate such that:

$$\begin{aligned} &\text{Common plane(s):} && (111)^{FCC} \parallel (12\bar{1})^{BCC} \text{ and} \\ &&& (1\bar{1}1)^{FCC} \parallel (\bar{1}21)^{BCC} \\ &\text{Common direction:} && [\bar{1}01]^{FCC} \parallel [\bar{1}0\bar{1}]^{BCC} \end{aligned}$$

Interestingly, for the given crystal orientations in grain 1, a second set of low index planes and directions was found to superpose as shown in **Figure 4B**. The common planes and directions are indexed and marked in red color with full and dotted circles, respectively.

$$\begin{aligned} &\text{Common plane(s):} && (1\bar{3}\bar{1})^{FCC} \parallel (\bar{1}03)^{BCC} \text{ and} \\ &&& (\bar{1}\bar{3}1)^{FCC} \parallel (\bar{3}01)^{BCC} \\ &\text{Common direction:} && [101]^{FCC} \parallel [010]^{BCC} \end{aligned}$$

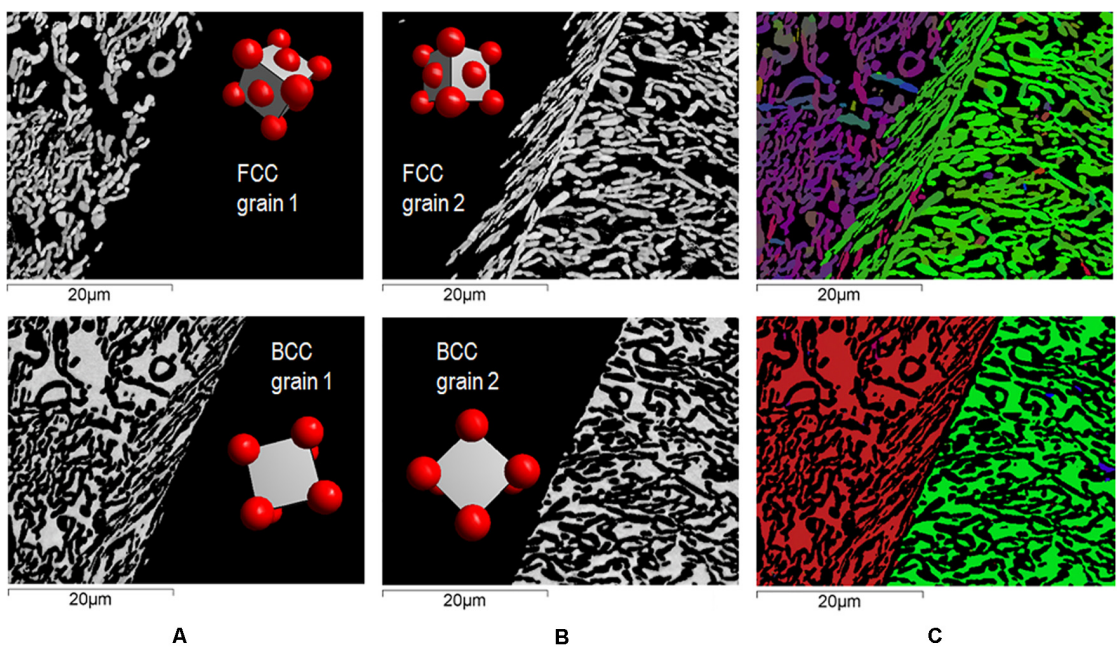

FIGURE 3 | EBSD map in sample $AlCrFe_2Ni_2$ with ultrafine vermicular microstructure in a region of interest containing a grain boundary of the parent BCC-B2 phase. The phases and their crystal mimic are shown for each grain **(A,B)**. An overall view is presented in **(C)** using an inverse pole figure color map for the FCC phase (top) and the BCC phase (bottom), respectively.

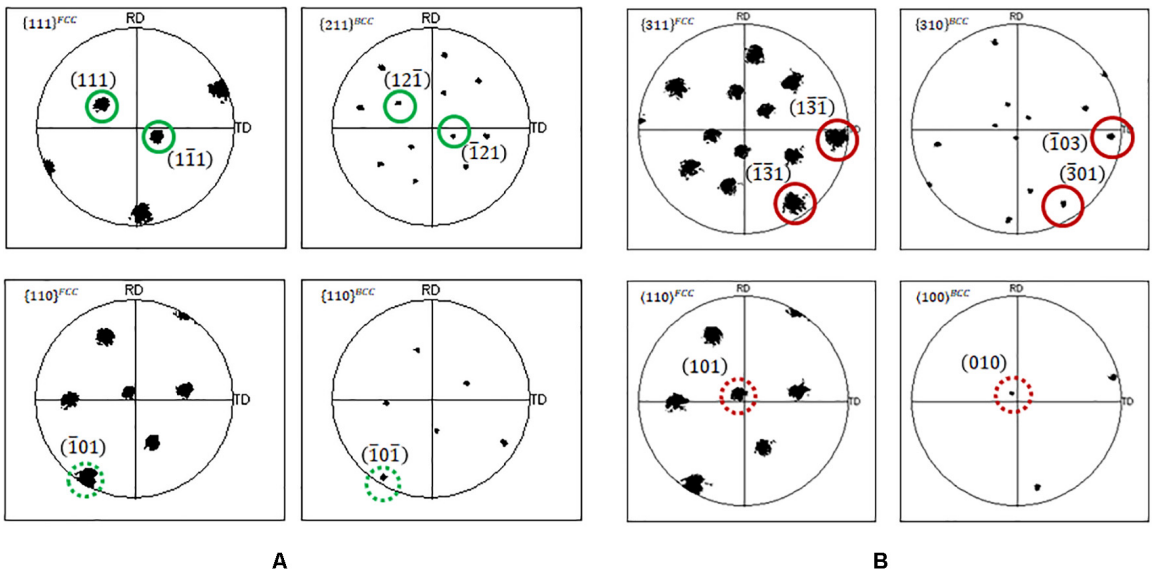

FIGURE 4 | Selected pole figures for grain 1, see **Figure 3A**, illustrating the primary **(A)** and the secondary **(B)** crystallographic orientation relationship between FCC and the parent BCC phase. Full circles mark the superposing poles, which correspond to the common planes. Dotted circles mark the superposing poles, which correspond to the common direction. Common planes and directions are indexed with the corresponding {hkl}-triplets.

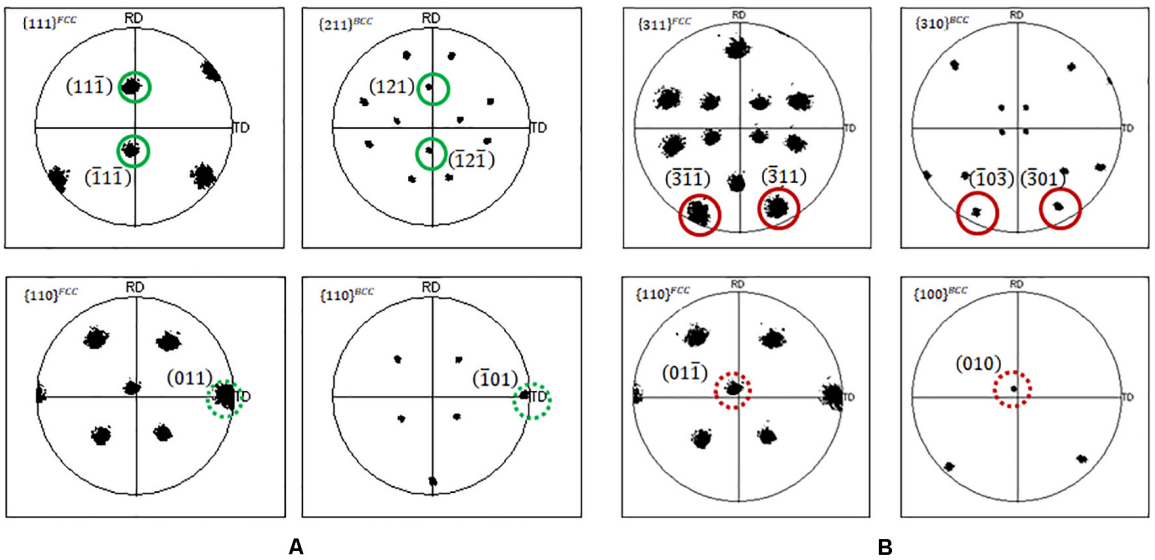

FIGURE 5 | Selected pole figures for grain 2, see **Figure 3B**, illustrating the primary **(A)** and the secondary **(B)** crystallographic orientation relationship between FCC and the parent BCC phase. Full circles mark the superposing poles, which correspond to the common planes. Dotted circles mark the superposing poles, which correspond to the common direction. Common planes and directions are indexed with the corresponding {hkl}-triplets.

Figures 5A,B confirm that the same ORs are present in grain 2, naturally with permuted {hkl}-indices for the common planes and directions. **Table 3** summarizes the results for both grains. The two ORs listed above are simultaneously valid and the system can choose to align phase boundaries to any of the common planes in order to reduce the phase boundary energy. For convenience, we call the ORs primary and secondary ORs. Likely, the primary OR provides deeper energy minima and more pronounced energy anisotropy compared to the secondary OR. The presence of the secondary and presumably less anisotropic OR may indeed explain the poor alinement of FCC/BCC interfaces observed in the ultrafine vermicular microstructures.

Noteworthy, the planes of the BCC phase pertaining to the above ORs are twinning planes, e.g., {112} and even {013}, as reviewed in Christian and Mahajan (1995). This suggests that twinning is possibly triggering the nucleation of vermicular FCC

TABLE 3 | Crystal orientation relationship(s) identified in an as-cast sample $AlCrFe_2Ni_2$ with ultrafine vermicular microstructure; the primary and secondary OR hold simultaneously.

No	EBSD map	Primary OR	Secondary OR
G1	Grain 1/**Figure 3**	$(111)^{FCC} \parallel (12\bar{1})^{BCC}$ $(1\bar{1}1)^{FCC} \parallel (\bar{1}21)^{BCC}$ $[\bar{1}01]^{FCC} \parallel [\bar{1}0\bar{1}]^{BCC}$	$(13\bar{1})^{FCC} \parallel (\bar{1}03)^{BCC}$ $(\bar{1}31)^{FCC} \parallel (\bar{3}01)^{BCC}$ $[101]^{FCC} \parallel [010]^{BCC}$
G2	Grain 2/**Figure 3**	$(11\bar{1})^{FCC} \parallel (121)^{BCC}$ $(\bar{1}1\bar{1})^{FCC} \parallel (\bar{1}2\bar{1})^{BCC}$ $[011]^{FCC} \parallel [\bar{1}01]^{BCC}$	$(\bar{3}1\bar{1})^{FCC} \parallel (\bar{1}0\bar{3})^{BCC}$ $(\bar{3}11)^{FCC} \parallel (\bar{3}01)^{BCC}$ $[01\bar{1}]^{FCC} \parallel [010]^{BCC}$
V1	Variant 1/**Figure 6**	$(\bar{1}1\bar{1})^{FCC} \parallel (211)^{BCC}$ $(111)^{FCC} \parallel (\bar{2}11)^{BCC}$ $[\bar{1}01]^{FCC} \parallel [01\bar{1}]^{BCC}$	$(13\bar{1})^{FCC} \parallel (013)^{BCC}$ $(\bar{1}31)^{FCC} \parallel (031)^{BCC}$ $[101]^{FCC} \parallel [\bar{1}00]^{BCC}$
V2	Variant 2/**Figure 6**	$(\bar{1}\bar{1}\bar{1})^{FCC} \parallel (21\bar{1})^{BCC}$ $(1\bar{1}1)^{FCC} \parallel (\bar{2}1\bar{1})^{BCC}$ $[\bar{1}01]^{FCC} \parallel [011]^{BCC}$	$(1\bar{3}\bar{1})^{FCC} \parallel (01\bar{3})^{BCC}$ $(\bar{1}31)^{FCC} \parallel (03\bar{1})^{BCC}$ $[101]^{FCC} \parallel [\bar{1}00]^{BCC}$
V3	Variant 3/**Figure 6**	$(111)^{FCC} \parallel (121)^{BCC}$ $(1\bar{1}1)^{FCC} \parallel (\bar{1}2\bar{1})^{BCC}$ $[10\bar{1}]^{FCC} \parallel [\bar{1}01]^{BCC}$	$(1\bar{3}\bar{1})^{FCC} \parallel (\bar{3}0\bar{1})^{BCC}$ $(\bar{1}31)^{FCC} \parallel (\bar{1}0\bar{3})^{BCC}$ $[101]^{FCC} \parallel [010]^{BCC}$

inside the spinodally decomposing BCC-B2 parent phase. The elastic strain associated with the compositional modulation may suffice to promote local twinning at the atomic level and trigger the BCC-FCC structural transition with these unusual ORs.

We observed, without showing details here, that nucleation events are, however, rare, meaning that vermicular domains within one single parent grain are large. In fact, these domains are crystallographic variants of the above given ORs. From a total of 12 possible variants we typically observe 3 to 4 variants in one parent grain. **Figure 6** shows an EBSD mapping region, which encompasses three vermicular domains evolved from the same parent grain. The phase map in **Figure 6A** shows the fractions of the two phases, with FCC reaching about 58 area%. **Figure 6B** shows the Euler map, with all Euler angles for both phases, **Figures 6C,D** show selected inverse pole figure color maps for BCC and FCC, respectively, being superposed to the pattern quality map. Finally, **Figure 6E** displays the crystal mimic of the parent BCC and of the three variants of the vermicular FCC

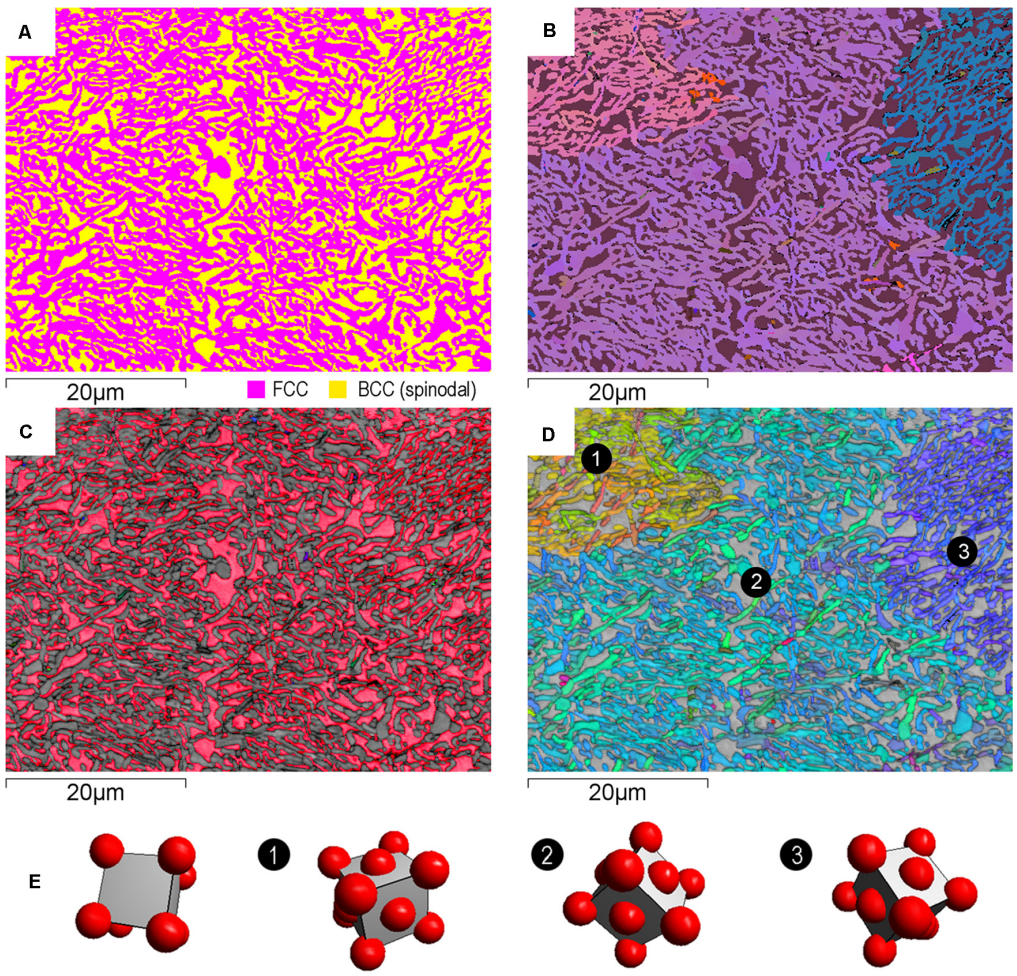

FIGURE 6 | EBSD map in sample $AlCrFe_2Ni_2$ with ultrafine vermicular microstructure in a region of interest containing three vermicular domains inside one parent BCC-B2 grain. The phase map **(A)** reveals the fraction of FCC ~58%. The Euler map **(B)** outlines the three distinct FCC domains. A better view of the phase orientation is given in the inverse pole figure color maps **(C,D)** superposed to the pattern quality maps. The crystal mimic of the phases in (E) shows the three FCC variants corresponding to the three vermicular domains. The full crystal OR is listed in **Table 3** for each variant.

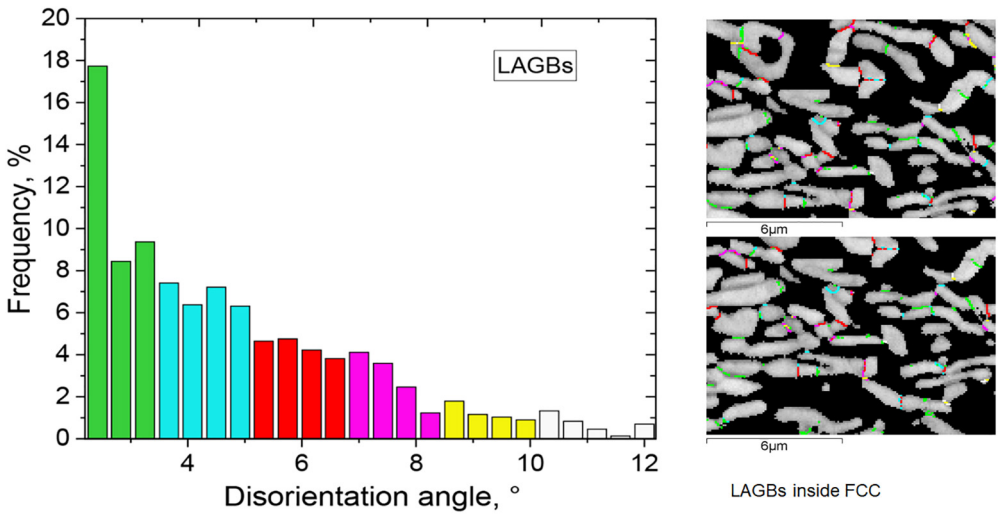

FIGURE 7 | Disorientation angle distribution inside the vermicular FCC phase of grain 2 (compare **Figures 3B,C**) in the range from 2 to 12° and associated sub-grain boundaries, i.e., low angle grain boundaries (LAGBs).

phase. **Table 3** lists the common planes and directions identified for each of the variants following the primary and secondary OR.

Finally, we recall that the vermicular FCC phase displays considerable lattice strain and a high density of low angle grain boundaries (LAGBs). These features result from the solid state phase transformation following the dynamic relaxation of phase transformation stresses accomplished through dislocation networks, dislocation slip, lattice rotations etc., which are known mechanisms of phase transformation plasticity (Denis et al., 1985). Due to the involved stresses, the elastoplastic deformation processes are complex, as shown by the simulations reported i.e., in Cottura et al., 2015 and Yamanaka et al., 2010 for other alloys. For the BCC-FCC transformation at case here, the spinodal decomposition of the parent phase induces yet another stress/strain field, which will affect the relaxation processes involved. From today's perspective, understanding the elastoplastic aspects of this solid state transformation and its impact on the observed lattice strain of the vermicular FCC phase is a true challenge.

A quantitative analysis of the lattice strain is beyond the scope of this paper. However, a convenient way to estimate the associated deformation is by analyzing the disorientation angle distribution inside the FCC phase (single grain including subgrains) using EBSD mapping data (Humphreys, 2001; Brough et al., 2006). The analysis is included in commercial EBSD software packages, here INCA Crystal. The relative disorientation (or misorientation) for a given data point is expressed as an angle-axis pair corresponding to the operation of rotating the crystal from each individual data point into coincidence with the average crystal orientation of the grain. The average disorientation angle is then calculated over all data points. The results are further used to outline low angle boundaries (LAGBs) according to predefined angular ranges. We illustrate the results of this analysis for the FCC-Grain 2 data (compare **Figure 3**) in **Figure 7**. The frequency of the measured disorientation angles are plotted for the range from 2 to 12° and color-coded for predefined ranges. LAGBs within the FCC phase are shown using the same color code. The average disorientation ranges around 5.8° being higher compared to a typical value of ∼3.8° found in a package of Widmanstätten laths. This rather high number reflects the lattice strain associated with the phase transformation when FCC growth occurs along with the spinodal decomposition of the parent BCC-B2 phase.

SUMMARY AND CONCLUSION

The spinodal decomposition of the BCC-B2 phase and more specifically its interaction with the BCC-FCC phase transformation is one of the most fascinating aspects in the alloy system Al-(Co)-Cr-Fe-Ni. In certain compositional regions, e.g., in alloys $Al_{0.8}CoCrFeNi$ and $AlCrFe_2Ni_2$, the sequence of phase transformations, involving the structural transformation BCC-B2 → FCC-A1 and the spinodal decomposition BCC-B2 → BCC-B2# + BCC-A2# change, when changing the cooling conditions. Three distinct phase transformation pathways are accessible, leading to very distinct microstructures.

- Upon slow cooling the classical Widmanstätten microstructure forms, however, with the remaining BCC phase being spinodally decomposed after completion of the BCC-B2 → FCC-A1 transformation.
- For moderate to high cooling rates an ultrafine vermicular microstructure forms with the FCC-A1 phase displaying a contiguous network, neatly interwoven with spinodally decomposed BCC. The thickness of the individual FCC "veins" is about the size of the spinodal wavelength. This structure is formed upon cooling into the three phase field "BCC-B2# + BCC-A2# + FCC-A1", i.e., when Widmanstätten growth is kinetically supressed due to the applied cooling conditions.

- For high and very high cooling rates the FCC formation can be fully supressed, leading to a metastable BCC spinodal state. It offers a high density of nucleation sites for FCC-A1 upon annealing in the three phase field "BCC-B2# + BCC-A2# + FCC-A1". The resulting morphology of FCC-A1 is best described by the term "micro-platelets" and it is unique because all crystallographic variants (Nishiyama-Wassermann) are present and randomly distributed within a parent grain.

In all cases, the phase fraction of FCC-A1 finally reaches about 50% to 60%, depending on the alloy composition. This nearly "duplex" phase balance makes these alloys very interesting for structural applications. Moreover, the distinct and unique microstructures described above are accessible along distinct manufacturing routes, e.g., sand casting, permanent mold casting, and additive manufacturing. Further research is needed to explore the mechanical properties associated to the distinct microstructures. Some properties, e.g., fatigue, will sensitively depend on the microstructural features, while other will show less pronounced dependency.

In the second part, we described the ultrafine vermicular microstructure in more detail, with emphasis on the crystal orientation relationship between FCC and BCC. The OR differs from Nishiyama-Wassermann and from any other BCC/FCC relationship known from literature on steels. It reads $\{111\}^{FCC} \parallel \{\bar{2}11\}^{BCC}$; $\bar{1}01^{FCC} \parallel 01\bar{1}^{BCC}$. A secondary, embedded OR reads $\{\bar{1}31\}^{FCC} \parallel \{031\}^{BCC}$; $101^{FCC} \parallel \bar{1}00^{BCC}$. The secondary and presumably less anisotropic OR may indeed explain the poor alinement of FCC/BCC interfaces observed in the ultrafine vermicular microstructures. Whether the OR is triggered by local twinning at the atomic level, remains to be investigated.

We finally emphasize that the phase transformations presented here and the associated microstructure features do not genuinely relate to high entropy or medium entropy effects as were originally postulated (Murty et al., 2014). They are a direct consequence of the thermodynamic equilibria of the alloy systems Al-Cr-Fe-Ni and Al-Co-Cr-Fe-Ni and the corresponding phase fields accessible by cooling. We note, however, that limited diffusion kinetics, if applicable (Divinski et al., 2018), may ease the transition to off-equilibrium transformation pathways, which in this case lead to very distinct microstructures. Our own research continues with focus on comparing the associated mechanical properties, specifically the fatigue resistance.

DATA AVAILABILITY STATEMENT

The raw data supporting the conclusions of this article will be made available by the authors, without undue reservation.

AUTHOR CONTRIBUTIONS

UH conducted the research and performed the analysis of crystal ORs. SG and OS prepared the samples by arc melting and performed EBSD measurements, as part of their Ph.D. research. EE performed TEM and STEM measurements including high resolution EDS measurements as part of his Ph.D. thesis. SO guided and supervised the research of EE. All authors contributed to the article and approved the submitted version.

FUNDING

The German Federal Ministry for Education and Research (BMBF) supported this research under grant number 03XP0163A in the frame of the M-era.Net Joint Call 2017, Project NADEA (no. 5129).

ACKNOWLEDGMENTS

EE and SO acknowledge funding through the Ministry of Science, Technology and Space, of the State of Israel in the frame of the M-era.Net Joint Call 2017, Project NADEA (no. 5129). We wish to thank Dimitrios Vogiatzief from Oerlikon AM GmbH for providing a sample from alloy $AlCrFe_2Ni_2$ in the as-build state, being produced by laser powder bed fusion.

REFERENCES

Abuzaid, W., and Sehitoglu, H. (2018). Plastic strain partitioning in dual phase Al13CoCrFeNi high entropy alloy. *Mater. Sci. Eng. A* 720, 238–247. doi: 10.1016/j.msea.2018.02.044

Bönisch, M., Wu, Y., and Sehitoglu, H. (2018). Twinning-induced strain hardening in dual-phase FeCoCrNiAl0.5 at room and cryogenic temperature. *Sci. Rep.* 8:10663. doi: 10.1038/s41598-018-28784-1

Brough, I., Bate, P. S., and Humphreys, F. J. (2006). Optimising the angular resolution of EBSD. *Mater. Sci. Technol.* 22, 1279–1286. doi: 10.1179/174328406X130902

Bunge, H. J., Weiss, W., Klein, H., Wcislak, L., Garbe, U., and Schneider, J. R. (2003). Orientation relationship of Widmannstätten plates in an iron meteorite measured with high-energy synchrotron radiation. *J. Appl. Crystallogr.* 36, 137–140. doi: 10.1107/S0021889802021386

Christian, J. W., and Mahajan, S. (1995). Deformation twinning. *Prog. Mater. Sci* 39, 1–157. doi: 10.1016/0079-6425(94)00007-7

Cottura, M., Benoît, A., Finel, A., and Le Bouar, Y. (2015). Plastic relaxation during diffusion-controlled growth of Widmanstätten plates. *Scripta Mat.* 108, 117–121. doi: 10.1016/j.scriptamat.2015.06.032

Da Silva, A. K., Ponge, D., Peng, Z., Inden, G., Lu, Y., Breen, A., et al. (2018). Phase nucleation through confined spinodal fluctuations at crystal defects evidenced in Fe-Mn alloys. *Nat. Commun.* 9, 1–11. doi: 10.1038/s41467-018-03591-4

De Jeer, L. T. H., Ocelík, V., and De Hosson, J. T. M. (2017). Orientation Relationships in Al0.7CoCrFeNi high-entropy alloy. *Microsc. Microanal.* 23, 905–915. doi: 10.1017/S1431927617012442

Denis, S., Aeby-Gautier, E., Simon, A., and Beck, G. (1985). Stress–phase-transformation interactions – basic principles, modelling, and calculation of internal stresses. *Mater. Sci. Technol.* 1, 805–814. doi: 10.1179/026708385790124071

Divinski, S. V., Pokoev, A., Neelamegan, E., and Paul, A. (2018). A mystery of "sluggish diffusion" in high-entropy alloys: the truth or a myth?. *Diffus. Fundam.* 17:69. doi: 10.4028/www.scientific.net/DF.17.69

Dong, Y., Gao, X., Lu, Y., Wang, T., and Li, T. (2016). A multi-component AlCrFe2Ni2 alloy with excellent mechanical properties. *Mater. Lett.* 169, 62–64. doi: 10.1016/j.matlet.2016.01.096

Gangireddy, S., Gwalani, B., Soni, V., Banerjee, R., and Mishra, R. S. (2019). Contrasting mechanical behavior in precipitation hardenable AlXCoCrFeNi high entropy alloy microstructures: single phase FCC vs. dual phase FCC-BCC. *Mat. Sci. Eng. A* 739, 158–166. doi: 10.1016/j.msea.2018.10.021

Humphreys, F. J. (2001). Review Grain and subgrain characterisation by electron backscatter diffraction. *J. Mater. Sci.* 36, 3833–3854. doi: 10.1023/A:1017973432592

Kao, Y. F., Chen, T. J., Chen, S. K., and Yeh, J. W. (2009). Microstructure and mechanical property of as-cast, -homogenized, and -deformed AlxCoCrFeNi (0 = x = 2) high-entropy alloys. *J. Alloys Compd.* 488, 57–64. doi: 10.1016/j.jallcom.2009.08.090

Knyazeva, M., and Pohl, M. (2013). Duplex steels: part I: genesis, formation, structure. *Metallogr. Microstruct. Anal.* 2, 113–121. doi: 10.1007/s13632-013-0066-8

Kurdjumow, G., and Sachs, G. (1930). Über den mechanismus der stahlhärtung. *Z. Phys.* 64, 325–343. doi: 10.1007/BF01397346

Li, C., Qu, Y., Zhang, Y., Lv, Q., and Qi, H. (2020). Effect of deep cryogenic treatment on the microstructure and mechanical properties of AlCrFe2Ni2 High-entropy alloy. *Mater. Res. Express* 7:036504. doi: 10.1088/2053-1591/ab7a5f

Linden, Y., Pinkas, M., Munitz, A., and Meshi, L. (2017). Long-period antiphase domains and short-range order in a B2 matrix of the AlCoCrFeNi high-entropy alloy. *Scr. Mater.* 139, 49–52. doi: 10.1016/j.scriptamat.2017.06.015

Loh, N. D., Sen, S., Bosman, M., Tan, S. F., Zhong, J., Nijhuis, C. A., et al. (2017). Multistep nucleation of nanocrystals in aqueous solution. *Nat. Chem.* 9, 77–82. doi: 10.1038/nchem.2618

Murty, B. S., Yeh, J. W., and Ranganathan, S. (2014). *High-Entropy Alloys*. Oxford: Butterworth-Heinemann.

Nishiyama, Z. (1934). X-ray investigation of the mechanism of the transformation from face centered cubic lattice to body centered cubic lattice. *Sci. Rep. Tohoku Imp. Univ.* 23:637.

Ohmori, Y., Nakai, K., Ohtsubo, H., and Isshiki, Y. (1995). Mechanism of widmanstätten austenite formation in a δ/γ duplex phase stainless steel. *ISIJ Int.* 35, 969–975. doi: 10.2355/isijinternational.35.969

Rao, J. C., Ocelík, V., Vainchtein, D., Tang, Z., Liaw, P. K., and De Hosson, J. T. M. (2016). The fcc-bcc crystallographic orientation relationship in AlxCoCrFeNi high-entropy alloys. *Mater. Lett.* 176, 29–32. doi: 10.1016/j.matlet.2016.04.086

Shi, Y., Yang, B., Xie, X., Brechtl, L., Dahmen, K. A., and Liaw, P. K. (2017). Corrosion of Al xCoCrFeNi high-entropy alloys: al-content and potential scan-rate dependent pitting behavior. *Corros. Sci.* 119, 33–45. doi: 10.1016/j.corsci.2017.02.019

Steurer, W. (2020). Single-phase high-entropy alloys – A critical update. *Mater. Charact.* 162:110179. doi: 10.1016/j.matchar.2020.110179

Tkaczyk, A. H., Bartl, A., Amato, A., Lapkovskis, V., and Petranikova, M. (2018). Sustainability evaluation of essential critical raw materials: cobalt, niobium, tungsten and rare earth elements. *J. Phys. D Appl. Phys.* 51:203001. doi: 10.1088/1361-6463/aaba99

Verbeken, K., Barbé, L., and Raabe, D. (2009). Evaluation of the crystallographic orientation relationships between FCC and BCC phases in TRIP steels. *ISIJ Int.* 49, 1601–1609. doi: 10.2355/isijinternational.49.1601

Wang, W. R., Wang, W. L., and Yeh, J. W. (2014). Phases, microstructure and mechanical properties of AlxCoCrFeNi high-entropy alloys at elevated temperatures. *J. Alloys Compd.* 589, 143–152. doi: 10.1016/j.jallcom.2013.11.084

Wassermann, G. (1935). *Über den Mechanismus der α-γ Umwandlung des Eisens Mitteilungen aus dem Kaiser-Wilhelm-Institut für Eisenforschung zu Düsseldorf*. Stuttgart: Verlag Stahleisen. doi: 10.1016/j.jallcom.2013.11.084

Yamanaka, A., Takaki, T., and Tomita, Y. (2010). Elastoplastic phase-field simulation of martensitic transformation with plastic deformation in polycrystal. *Int. J. Mech. Sci.* 52, 245–250. doi: 10.1016/j.ijmecsci.2009.09.020

Conflict of Interest: The authors declare that the research was conducted in the absence of any commercial or financial relationships that could be construed as a potential conflict of interest.